Phys. Med. Biol. 39 (1994) 1721–1744. Printed in the UK

Pulsed photothermal radiometry in optically transparent media containing discrete optical absorbers

I A Vitkin†, B C Wilson‡, R R Anderson§ and S A Prahl‖

† Department of Medical Physics, Hamilton Regional Cancer Centre and McMaster University, Hamilton, Ontario, Canada L8V 1C3

‡ Department of Clinical Physics, Ontario Cancer Institute/Princess Margaret Hospital and Department of Medical Biophysics, University of Toronto, Toronto, Ontario, Canada M4X 1K9

§ Wellman Research Laboratories of Photomedicine, Massachusetts General Hospital, Boston, MA 02114, USA

‖ Department of Electrical Engineering and Applied Physics, Oregon Graduate Institute, Portland, OR 97271-1000, USA

Received 24 May 1994

Abstract. A description of heat transport by conduction and radiation in inhomogeneous materials following absorption of a brief optical pulse is presented, and investigated experimentally using pulsed photothermal radiometry (PPTR). The model indicates that the role of radiation as an intramedium heat transfer modality increases with increasing temperatures and decreasing infrared (IR) absorption of the medium. However, for the range of conditions analysed in this study, conductive transfer dominates. Thus, the inclusion of radiation does not significantly perturb the internal temperature profiles, although it does influence the radiometric emission from the sample, and hence the PPTR signal. The thermal confinement effects described in this study may be relevant in photomedicine, for example in pulsed laser irradiation of tissues containing small absorbing targets.

1. Introduction

Pulsed photothermal radiometry (PPTR) is a remote sensing technique that uses an infrared (IR) detector to monitor the transient increase in thermal radiative emission induced by absorption of pulsed optical radiation (Tam and Sullivan 1983, Imhof *et al* 1984). Physical parameters such as optical absorption and scattering coefficients (Prahl *et al* 1992), thermal diffusivity (Leung and Tam 1983), and thermal conductivity (Leung and Tam 1988) can be obtained by analysing the shape of the emission–time curve. Because of its non-contact nature, relative insensitivity to geometrical alignment of the sample, and ability to examine opaque materials, PPTR has seen some biomedical applications (see, for example, Vitkin *et al* (1994a) and references therein). Typically, theoretical models of PPTR use conductive heat transfer to describe the evolution of the temperature field in the sample following the optical pulse. However, when the locally induced temperature excursions become significant (greater than several hundred degrees Celsius) thermal radiation becomes increasingly efficient as a mode of heat transfer, and the temperature field in the material may be influenced by its presence. Quantitative analysis of this effect is very challenging, involving simultaneous conduction and radiation heat transfer. In most circumstances, PPTR is primarily used as a non-destructive characterization technique, the transient temperature

0031-9155/94/101721+24$19.50

jumps in bulk media with uniformly dispersed absorption are limited to $\sim$ 10–20 °C, and radiative transfer need not be invoked (Tom *et al* 1982).

In this study, we have investigated a system whose PPTR signals differ greatly from those previously reported in the literature, namely one in which the optical energy absorption is localized at discrete centres within the medium, resulting in large localized temperature jumps. By suspending highly absorbing carbon-black particles in an optically transparent water-based gel, and irradiating the composite phantom with a brief laser pulse, the generated temperature differences between the absorbing particles and the transparent surrounding gel are shown to be at least several hundred degrees Celsius. Hence, radiative heat transfer influences the heat transfer dynamics within the medium, and affects the shape of the PPTR signal. Such models may be relevant, for example, to specific biomedical applications of pulsed lasers, such as ocular interventions involving the retinal pigment epithelium (Roider *et al* 1992) or the trabecular meshwork (Kobsa *et al* 1989), and melanosome targeting and tattoo removal in dermatology (Polla *et al* 1987, Vance *et al* 1985, Taylor *et al* 1990). These medical procedures are often optimized using the concept of selective photothermolysis (Anderson and Parrish 1983), which achieves target selectivity by using a preferentially absorbed laser pulse shorter than the thermal relaxation time of the absorber. This time is calculated based on heat conduction effects only. However, with very small discrete absorbers such as melanosomes or pigmented particles, extremely high spatially localized temperatures are produced following irradiation with sub-microsecond pulses. In this setting, it is important to understand the potential role played by thermal radiative transfer within the medium. The model developed in this paper is intended to examine this issue, and to enable quantitative PPTR investigations in cases where this role may be significant.

Our general theoretical approach is to model the spatio-temporal dependence of the temperature field, $T(r, t)$, in a medium with both conductive and radiative heat transfer mechanisms. We initiate the calculations at the time immediately following the absorption of a brief laser pulse by the particulate absorbers. From $T(r, t)$, we then calculate the IR emission from the medium as a function of time, and compare these results with PPTR signals measured experimentally by an IR detector viewing the centre of the irradiated area on the surface of the medium.

2. Theory

2.1. Basic equations

Analysis of combined transient conduction and radiation transfer following a brief laser pulse involves two coupled differential equations. First, at any point in the medium, energy conservation gives

$$\rho c \partial T/\partial t = -\nabla(-k\nabla T + F) \tag{1}$$

where ρ is the density, c is the specific heat, k is the thermal conductivity, t is the time, T is the temperature, and F is the thermal radiative flux (power per unit area). F can be obtained by integrating the radiative intensity distribution I (power per unit area per solid angle) over the appropriate direction in space:

$$F = \int_{4\pi} I \cos\theta \, \mathrm{d}\Omega \tag{2}$$

where θ and Ω are the polar and the solid angle, respectively. The intensity, in turn, is obtained from the solution of the radiative transfer equation (Chandrasekhar 1950, Ozisik 1973), an integro-differential equation that contains a temperature-dependent black-body term as a source:

$$\bar{\Omega}\nabla I = -(\mu_a + \mu_s)I + \int \mu_s(\Omega' \to \Omega)I \, d\Omega' + \mu_a I_{BB}(T^4). \tag{3}$$

In (3), the term on the right-hand side represents the loss due to absorption and scattering, with μ_a the linear absorption coefficient of the medium and μ_s the linear scattering coefficient, both averaged over the (primarily IR) wavelengths of the radiative intensity distribution. The second term is the gain due to in-scattering, and the last term is the augmentation of intensity due to the emission of thermal IR radiation by the material in the direction Ω. For an ideal black body, this emission varies as the fourth power of absolute temperature when integrated over all energies; for a real emitter, the integration is more problematic because of the presence of absorbing and transmitting bands in its energy spectrum, detailed knowledge of which is generally inadequate. Nevertheless, the result is still taken to be proportional to the fourth power of temperature, with emissivity, $\varepsilon < 1$, introduced to account for the decreased emission compared to the ideal (black-body) radiator. Thus, determining the temperature field in the material under the conditions of simultaneous conductive and radiative transfer requires solving the two coupled equations (1) and (3). Although some approximate solutions have been obtained (Ozisik 1973, Viskanta and Hirleman 1978, Siegel and Howell 1988, Brewster 1992), the transient solution in an arbitrary geometry has proven very difficult. Thus, we simplify the formulation by assuming that the scattering of thermal radiation is negligible compared to absorption, a common and accurate assumption in systems where the scattering coefficient is smaller or even equal to the absorption coefficient (Goody and Yung 1989). This is certainly applicable to an IR absorber as strong as water and, hence, probably true of most soft tissues. Then, (3) predicts that the local spatial gradient of radiative intensity is equal to the difference between IR emission and absorption (the former depends on the local temperature; the latter depends on the thermal emission and, therefore, temperature of the surrounding medium). This treatment of the radiative term enables the numerical solution of the energy equation using a finite-difference formulation, as below.

For algebraic simplicity and clarity of presentation, we make a number of assumptions. Firstly, instead of working in three dimensions as suggested in the experimental case, figure 1(a), we assume that the incident light, and the conductive and thermal radiative fluxes, depend on depth in the medium only. This amounts to replacing the 'hot centres' of figure 1(a) with the 'hot planes' of figure 1(b), and assuming that heat transfer is in the x direction only. Secondly, as mentioned above, we ignore scattering since $\mu_a \gg \mu_s$ for tissue in the spectral region of greatest IR emission. Thirdly, we assume that most of the material properties (except for the thermal conductivity of water and the heat transfer coefficient at the medium–air interface) are temperature independent.

The method of solution consists of dividing the medium into a number of smaller slabs of thickness Δx, as in the classical finite-difference formulation. By virtue of its temperature, each element emits a specified amount of radiative energy, split equally into the positive and negative x directions. It also received radiant emission from all other elements on both sides, attenuated by the absorption in the medium by the factor $\exp(-\mu_{IR}d)$, where d is the distance from the origin of the radiant flux to the element in question, and μ_{IR} is the absorption coefficient of the medium. Note that we have also changed the subscript on the absorption coefficient to emphasize the fact that the absorption and emission phenomena

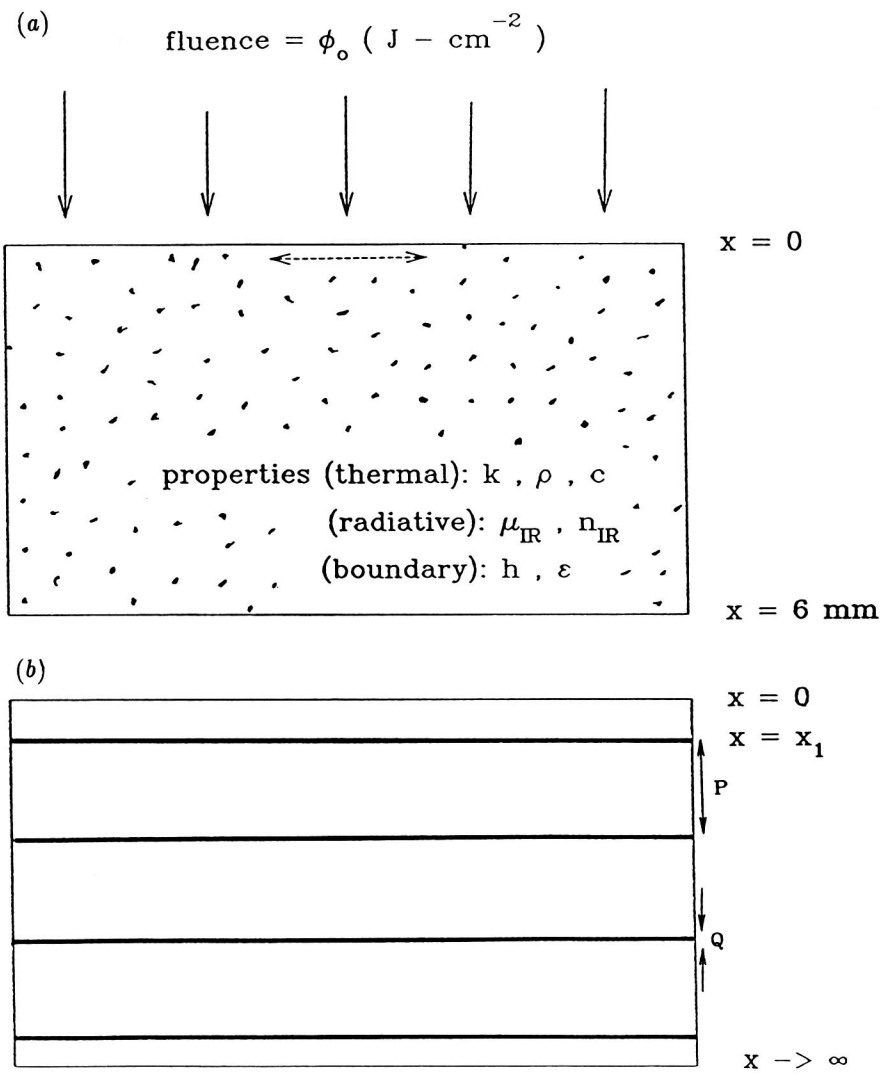

Figure 1. (a) A schematic diagram of the experimental phantom containing discrete absorbing centres in an optically transparent medium, subject to wide-beam irradiation at the top surface. The dotted horizontal arrow denotes the central region whose thermal emission is monitored by the IR detector. (b) The corresponding one-dimensional geometry used in the theoretical model.

under discussion occur primarily in the IR region of the electromagnetic spectrum. Rewriting (1) in finite-difference form, we have the following relation for the temperature T at time t:

$$\rho c(T_i' - T_i)/\Delta t = (k/\Delta x^2)[T_{i-1} - 2T_i + T_{i+1}] + (1/\Delta x)[F_{ab}(i) - F_{em}(i)] \tag{4}$$

where $i = 1, 2, 3 \ldots$ refers to the element number, Δt is the time increment, and T' is the temperature at time $t + \Delta t$. The net radiative flux emitted from the ith element is (Sparrow and Cess 1978, Al Abed and Sacadura 1983, Atalla and Hasan 1986)

$$F_{em}(i) = 4\pi[\mu_{IR}(i)\Delta x \sigma T_i^4 n_{IR}^2]/\pi = 4\mu_{IR}(i)\Delta x \sigma n_{IR}^2 T_i^4 \tag{5}$$

where n_{IR} is the infrared index of refraction of the medium surrounding the element in question. Similarly, the flux absorbed by the ith element is due to the emissions of all its neighbours:

$$F_{ab}(i) = \mu_{IR}(i)\Delta x \sum_{j=-\infty}^{j=+\infty} F_{em}(j)e^{-\mu_{IR}(i,j)|i-j|\Delta x} \qquad j \neq i \tag{6}$$

where $\mu_{IR}(i, j)$ is the spatially dependent absorption coefficient between nodes i and j. The use of different values of μ_{IR} allows us to incorporate the different radiative properties of the particulates and of the surrounding media. However, since the samples examined in this study were $\sim 98\%$ water, and the IR properties of the particulate inclusions are assumed to be similar to it, we will take the IR absorption coefficient as constant throughout the medium for most simulations. An exception will be made when we examine the effect of the radiative properties of the medium, which are varied while μ_{IR} of the inclusions is kept fixed (see the discussion concerning figure 5). Then, using the definition of the transmissivity function along a line of sight ab, $\tau(a, b) = \exp(-\mu_{IR}|a - b|)$, the last equation can be rewritten in a computationally convenient form as (Brewster 1992)

$$\begin{aligned} F_{ab}(i) &= (\mu_{IR}(i)\Delta x) \sum_{j=i-N}^{j=i+N} 4\sigma T_j^4 n_{IR}^2 [\tau(j, i) - \tau(j-1, i)] \\ &= (\mu_{IR}(i)\Delta x)\Bigg\{ \sum_{j=i-N}^{i} 2\sigma T_j^4 n_{IR}^2 [\tau(j, i) - \tau(j-1, i)] \\ &\quad + \sum_{j=i+1}^{i+N} 2\sigma T_j^4 n_{IR}^2 [\tau(j, i) - \tau(j-1, i)]\Bigg\} \end{aligned} \tag{7}$$

where $N = 0, 1, 2, \ldots$ is the number of elements that separate the emission node j from the absorption node i. The resulting equations describe the simultaneous conductive and radiative transfer in the medium.

In order to complete the formulation, we need to specify the boundary and the initial conditions. At the sample–air interface, energy is transferred by convection and radiation. The instantaneous energy balance at the interface can be expressed as

$$k\frac{\delta T}{\delta x} = h(T_l - T_a) - \left(\sum_{j=2}^{N} F_{em}(j)[\tau(j, 1) - \tau(j-1, 1)] - \sigma T_a^4 \right) \qquad x = 0 \tag{8}$$

where h is the convective heat transfer coefficient, and T_l and T_a are the sample surface and the ambient air temperatures, respectively. The radiative term includes the flux emitted from subsurface elements, attenuated according to their distance from the surface. This is more accurate than having the outgoing emitted flux simply originate at the surface ($i = 1$) element. The radiometric signal seen by the IR detector will be proportional to this term, that is

$$S(t) \sim \sum_{j=2}^{N} F_{em}(j, t)[\tau(j, 1) - \tau(j-1, 1)]. \tag{9}$$

The initial temperature, $T(x, t = 0)$, is assumed to be equal to T_0 throughout the medium, except at the location of the heated absorbing granules. There, its spatial extent is equal

to the granule diameter, and its magnitude is T_h. Thus, the initial temperature field has a picket-fence profile, with the absorbing centres accounting for the height and the location of the pickets. The location of the first picket and the repeat distance (corresponding to the percentage loading of the absorbing granules) are specified at the start of the simulation. Light scattering and heat loss during the laser pulse will influence the initial temperature field; these effects will be described later.

2.2. Numerical solution

The formulation presented above was simulated on a digital computer (IBM 486) using the values of the parameters summarized in table 1. As the volume content of the absorbing pigment was very small (< 3%), the bulk properties of the medium were assumed to be equal to those of water. (4) was solved using an explicitly finite-difference scheme. This is best suited for predictions of early-time behaviour. Unfortunately, it is difficult for any given method to be well suited for both early-time and late-time calculations (Sutton 1986), but we are interested in signal dependence for all times. Thus, the time step chosen (viz. 1 μs) was close to the maximum allowed by stability considerations (Gerald and Wheatley 1984, Arpaci 1962), and was confirmed by halving the time step and ensuring the solution results did not change. The slab was divided into 1000 evenly spaced elements (1001 nodes). In addition to the variables listed in table 1, the input to a particular simulation specified the location of the first hot centre (at position x_1), the relative abundance of the hot centres (a pigment layer every P elements), the size of the hot centre (Q elements), the magnitude of T_h, and the value of μ_{IR}. The element at position x_1 and $Q/2$ of its neighbours on both sides were assigned the temperature T_h (see figure 1(b)). This procedure was repeated every P elements until $i = 1000$ was reached. All other locations in the medium had initial temperature T_0. Then, the absorption matrix was calculated using (7) for $i = 1, 2, \ldots, 950$, where we assume that events deeper in the medium will not be manifest at the surface. The value of N in that equation depends on the product $\mu_{IR}\Delta x$, and was generally ~ 30. It was selected so that the sum

$$\sum_{m=|i-j|=1}^{N} e^{-m(\mu_{IR}\Delta x)} \tag{10}$$

was within 0.3% of its value when $N = \infty$. Then, (4) was solved throughout the medium for the temperatures at the next time step, the radiation escaping from the surface was tabulated as $S(t)$ according to (9), and the entire procedure repeated. As a consistency check, T_h was put equal to T_0 for all elements, and the simulation executed for 5000 time steps. The temperature everywhere remained equal to T_0 within the double-precision limit of the computer.

Figure 2 shows an example of the thermal radiative emission from the sample surface (left ordinate), to be compared to the measured PPTR signals described later. Also plotted is the temperature at the centre of an absorbing layer at a position deep within the medium (right ordinate). Examining the signal behaviour first, we note the very sharp peak at early time (height $\sim$ 321 units at $t \sim 1$ μs, FWHM ~ 5 μs) followed by a fast decrease, then a more gradual rise to a second peak at ~ 3 ms, and a slow monotonic decay thereafter. The last feature is reminiscent of conductive heat transfer as confirmed by numerous PPTR measurements (Tam and Sullivan 1983, Prahl *et al* 1992), and is probably indicative of the cooling of the entire layer once the extreme temperature gradients within it have been smoothed out. We postulate that the initial sharp peak is caused by the direct thermal radiation from the heated granules close to the surface, the extent of the depth contribution

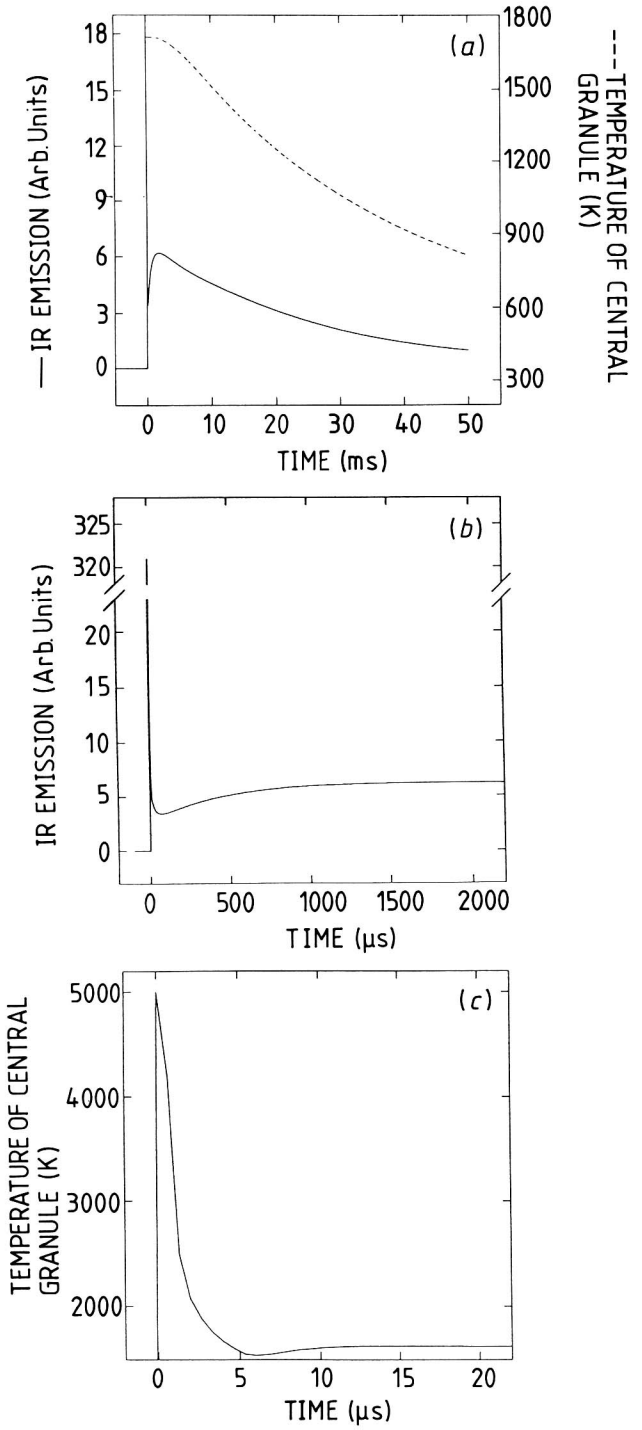

Figure 2. (a) The predicted thermal radiative emission (left ordinate) and the temperature at the mid-point of a centrally located hot centre (right ordinate) as functions of cooling time: Initial hot-centre temperature, 5000 K; IR absorption coefficient, 1000 cm^{-1}. All other parameters used in the simulation are as in table 1. (b) An expanded view of the initial signal peak. (c) An expanded view of the initial temperature.

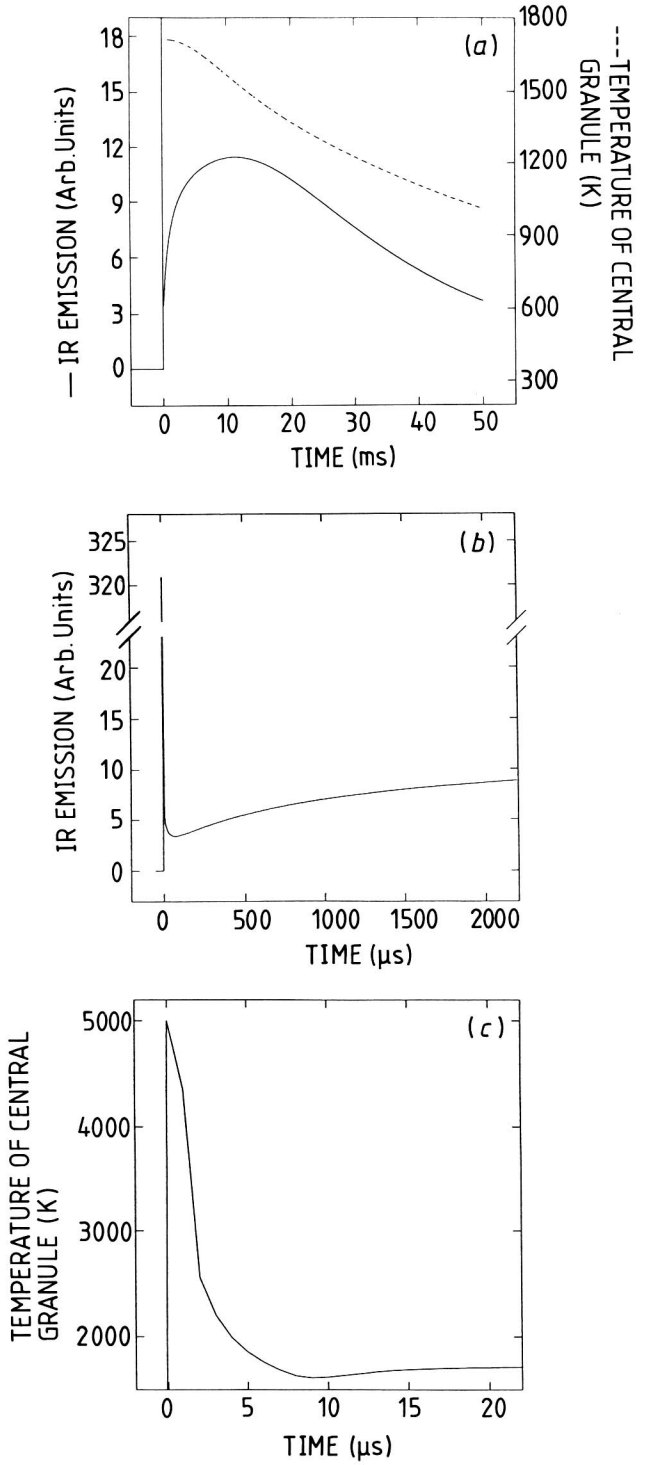

Figure 3. (a) The effect of neglecting intramedium radiative transfer. The conditions are the same as in figure 2, except that heat exchange is by conduction only. (b) An expanded view of the initial signal peak. (c) An expanded view of the initial temperature.

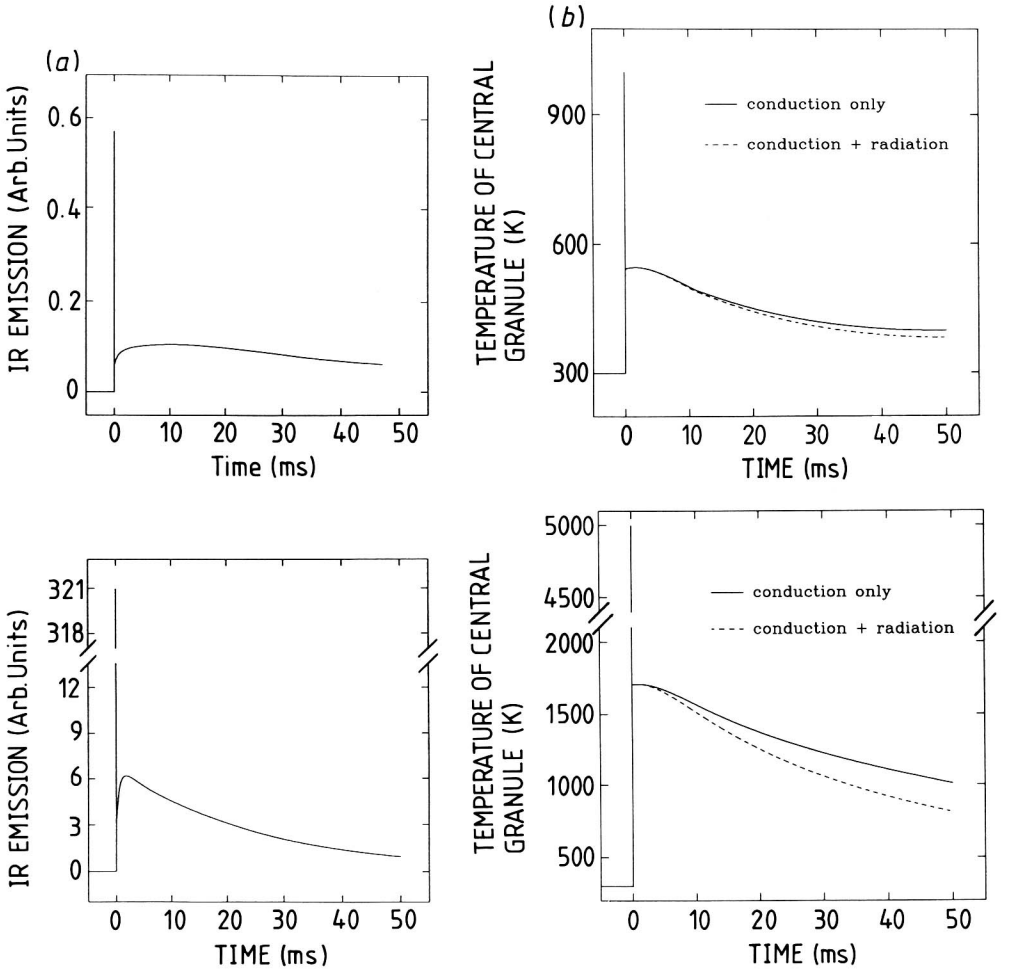

Figure 4. The effect of varying the initial hot-centre temperature, T_h, with conductive–radiative transfer. (a) A comparison of IR emissions, with $T_h = 1000$ K (top) and $T_h = 5000$ K (bottom). (b) The temperature of a deeply located hot centre with and without radiative transfer, with $T_h = 1000$ K (top) and $T_h = 5000$ K (bottom). $\mu_{IR} = 1000$ cm^{-1}.

being dictated by the magnitude of the absorption coefficient μ_{IR}. The appearance of the second peak is more puzzling, for it seems to suggest an arrival of a delayed thermal wave. In this model, such a wave cannot be due to scattering effects or layered structures, two instances that can cause a delayed PPTR peak (Vitkin *et al* 1994b). We interpret it as indicating that the heated particles close to the surface have been quickly (of the order of microseconds) and efficiently cooled by radiative emission to the environment, whereas the emissions from the deeper layers have been reabsorbed in the medium. In such a scenario, the effective temperature of the deeper layers is higher than that of the radiatively cooled surface layers shortly after the pulse. This borne out by the fact that the centrally positioned granule is always at a higher temperature than the one close to the surface during the simulations. Thus, there results a time-delayed thermal wave arriving at the surface by a

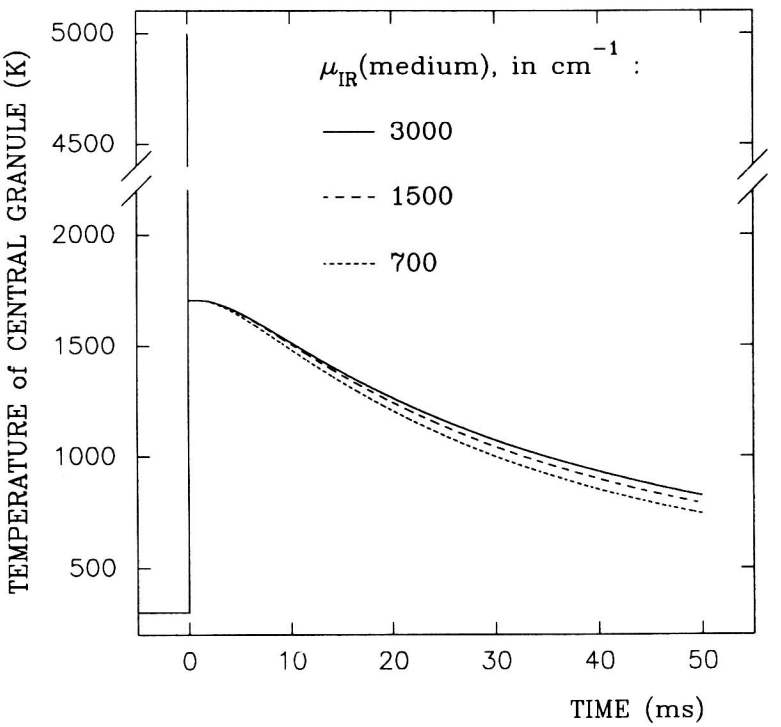

Figure 5. The effect of varying the medium absorption coefficient, μ_{IR}, with conductive–radiative transfer. $T_h = 5000$ K, μ_{IR}(hot centres) = 1000 cm^{-1}.

Table 1. Parameter values used in generating figures 2–5. The thermophysical and optical properties are those of water.

Thermal conductivity, k	~ 0.0056 W cm^{-1} K^{-1}:$f(T)$[a]
Density, ρ	1 g cm^{-3}
Specific heat, c	4.184 J g^{-1} K^{-1}
Surface heat transfer coefficient, h	~ 0.001 W cm^{-2} K^{-1}:$f(T_{surface})$[b]
IR refractive index, n_{IR}	1.3
Ambient temperature, T_a	300 K
Initial medium temperature, T_0	300 K
Time increment, Δt	10^{-6} s
Element thickness, Δx	10^{-4} cm
Initial width of a hot centre	3 μm (three elements wide)
Relative abundance of hot centres	10% (3 μm wide hot centre every 30 μm)
Initial hot-centre temperature, T_h	1000–5000 K
IR absorption coefficient of medium, μ_{IR}	700–3000 cm^{-1}

[a] For $T < 600$ K, $k(T) = -5.39 \times 10^{-3} + 6.38 \times 10^{-5}T - 7.99 \times 10^{-8}T^2$ (least-squares fit to data tables of Weast and Astle (1983)). For $T > 600$ K, $k(T) = 0.006$.

[b] $h(T_s < 400\text{ K}) = 0.0006$; $h(T_s > 400\text{ K}) = 0.0008$; $h(T_s > 500\text{ K}) = 0.001$; $h(T_s > 600\text{ K}) = 0.004$, where T_s is the temperature of the surface node (Weast and Astle 1983).

relatively slow (of the order of milliseconds) conduction process. What is interesting is the role played by *intramedium thermal radiative transfer* in the overall heat transfer process.

The thermal history of the hot centre also shows the fast peak followed by a more gradual

monotonic decay. The abrupt transition from a fast-cooling to a slow-cooling regime (at $t \sim 20$ μs, and $T \sim 1660$ K) is due to the presence of the other hot centres in the vicinity of the particle; in their absence, the hot centre continues its fast monotonic decay (confirmed by simulations with only one hot-centre particle present).

In order to ascertain the role of radiative heat transfer in the cooling process of the hot centre, we repeated the simulation under identical conditions, with heat transfer occurring by conduction only. The radiative term was retained only near the boundary, where it was used to calculate the signal magnitude via (9). Figure 3 demonstrates the resultant signal and the temperature history of a central hot node. The signal and temperature profiles are qualitatively similar to figure 2, but differ in quantitative detail. Notice, for example, that the hot-centre temperature profile is slightly lower under the conduction–radiation conditions than under the conduction-only scenario. This is due to the additional heat lost by radiation. As for the signal comparison, there is a significant difference in the magnitude and in the arrival time of the delayed thermal wave. The conduction-only signal is generally higher and arrives later at the surface than if radiative transfer is included. This is probably because the temperature distribution in the sample with radiative transfer becomes uniform somewhat faster than by conduction alone. Thus the top layer, whose temperature is primarily responsible for the thermal IR emission, registers the presence of the deeper hot spots faster in figure 2 than in figure 3, and its second-peak signal and the hot-spot temperatures are lower (indicative of a more uniform temperature profile in the medium).

Figure 4 demonstrates the effect of the variable T_h on the IR signal. Since the magnitude of the thermal emission is highly dependent on temperature ($\sim T^4$), the radiative-emission signal is higher for the higher-temperature simulation. In fact, if we compare the peak values of figure 4(a), we find $(321/0.6)^{1/4} \sim 5$, as expected from the ratio of the initial hot-centre temperatures. Moreover, the thermal gradients in the medium become more pronounced with higher hot-centre temperatures, so the importance of radiative transfer in homogenizing the temperature distribution increases. This was evident from comparing temperatures of the hot centres in the absence of radiation for the two T_h cases (part (b) of figure 4): the radiation caused a larger increase in the cooling rate for higher initial temperature, although the effect was relatively minor in both instances.

Figure 5 shows the effects of varying μ_{IR} of the medium. For these simulations, the IR absorption coefficient of the hot centres was kept constant at 1000 cm^{-1} to ensure that their thermal emission was constant, and the effects observed were entirely due the IR absorption properties of the surrounding medium. The hot centre cools faster with decreasing absorption coefficient of the surrounding medium, indicating that more energy is lost to the surrounding medium/external environment *via* thermal emission. This is because a small absorption coefficient represents a large radiative interaction distance; i.e., as the medium becomes more transparent in the IR, radiative exchange between the emitting centres is less impeded by the intervening medium, and their temperature drops. On the other hand, large μ_{IR} means short reabsorption distance, so the medium offers a large effective resistance to radiative cooling. It should also be noted that the simulation times increase significantly for small μ_{IR} values, since more terms must be evaluated in the radiative emission sum (see (10)).

In general, the relative importance of the two modes of energy transport can be expressed by a non-dimensional quantity known as the radiation-to-conduction parameter, M_i. Consider two emitting surfaces at temperatures T_1 and T_2, separated by a medium with properties k, μ_{IR}, and n_{IR}. For a radiatively thick medium, M_i is given as (Ozisik 1973, Brewster 1992)

$$M_i = 4n_{IR}^2 \sigma T_i^3 / k\mu_{IR} \tag{11}$$

where the subscript is based on a particular temperature T_i (either T_1 or T_2). For $M_i \to \infty$ radiative energy transfer dominates (radiation alone establishes the temperature field), and for $M_i \to 0$ conduction dominates. In figures 2–5, M_i ranged from ~ 0.007 to ~ 1.3, with the most common set of examined conditions ($T_h = 5000$ K, $\mu_{IR} = 1000$ cm^{-1}) yielding $M_i \sim 0.9$. As (11) and figures 4 and 5 demonstrate, the importance of the radiative contribution increases with increasing temperatures and decreasing IR absorption. (In analogy with thermal conductivity, radiative conductivity can be defined for radiatively thick media, $k_{rad} = 16n^2\sigma T^3/3\mu_{IR}$ (Ozisik 1973), which summarizes the importance of temperature and IR absorption coefficient for effective radiative contribution to heat transfer). Likewise, the role of conduction diminishes with decreasing values of thermal conductivity.

Finally, we examine the temperatures and the IR emission when thermal transfer occurs in three dimensions, using Cartesian coordinates (x, y, z), in order to ascertain whether the simplified 1D representation is adequate for comparison with PPTR experiments. In three dimensions (4) takes the form

$$\rho c(T'_{i,j,k} - T_{i,j,k})/\Delta t = (k/\Delta l^2)[T_{i-1,j,k} + T_{i+1,j,k} + T_{i,j-1,k} + T_{i,j+1,k} + T_{i,j,k-1} + T_{i,j,k+1} - 6T_{i,j,k}] + (1/\Delta l)[F_{ab}(i, j, k) - F_{em}(i, j, k)] \tag{12}$$

where $\Delta l = \Delta x = \Delta y = \Delta z$ is the element length. The directional emission terms now become

$$F_{em}(i, j, k)|_{\bar{x}} = [4\mu_{IR}(i, j, k)\Delta l \sigma n_{IR}^2 T_{i,j,k}^4]/3 \tag{13}$$

in the x direction, and similarly in the y and z directions. The absorption term is similarly modified to account for the six fluxes incident on a given volume element. The boundary formulation remains similar to that in (8). Analogous to the 1D case, (13) was solved using an explicit finite-difference scheme. The simulation was performed on a Micro-VAX 4400. The matrix size was $70 \times 70 \times 70$ nodal points. The coordinates of the central nodes of hot centres were selected randomly in the x–y–z space, subject to the constraint that they be nine nodes apart; then the six adjacent nodes are also assigned the temperature T_h, and all other nodes are initiated with the temperature 300 K. This corresponds to $\sim 1\%$ vol/vol loading of 3 μm diameter particles, to be compared directly with subsequent experimental PPTR results. Other inputs were $\mu_{IR} = 1000$ cm^{-1} and $T_h = 5000$ K. The tabulated IR signal represents the emission from a 20 node×20 node area centrally located at the surface. The results in figure 6 show the same signal features as seen previously, illustrating that 1D modelling is adequate for qualitative comparison with the experiments.

3. Experimental details

The details of the photothermal transfer dynamics were studied using PPTR. Figure 7 shows a schematic diagram of the experimental arrangement, which has been described previously (Prahl *et al* 1992). Briefly, a Q-switched ruby laser (Lasermetrics 939R3L) delivered 694 nm pulses of 50 ns duration. The emerging light was directed through a 7 mm diameter aperture for spatial filtering, passed through a confocal doublet lens pair (Galilean telescope), and was focused onto the sample surface at 10° from the normal. This resulted in a nearly uniform beam (±15%) of about 5 mm diameter. The incident fluence was

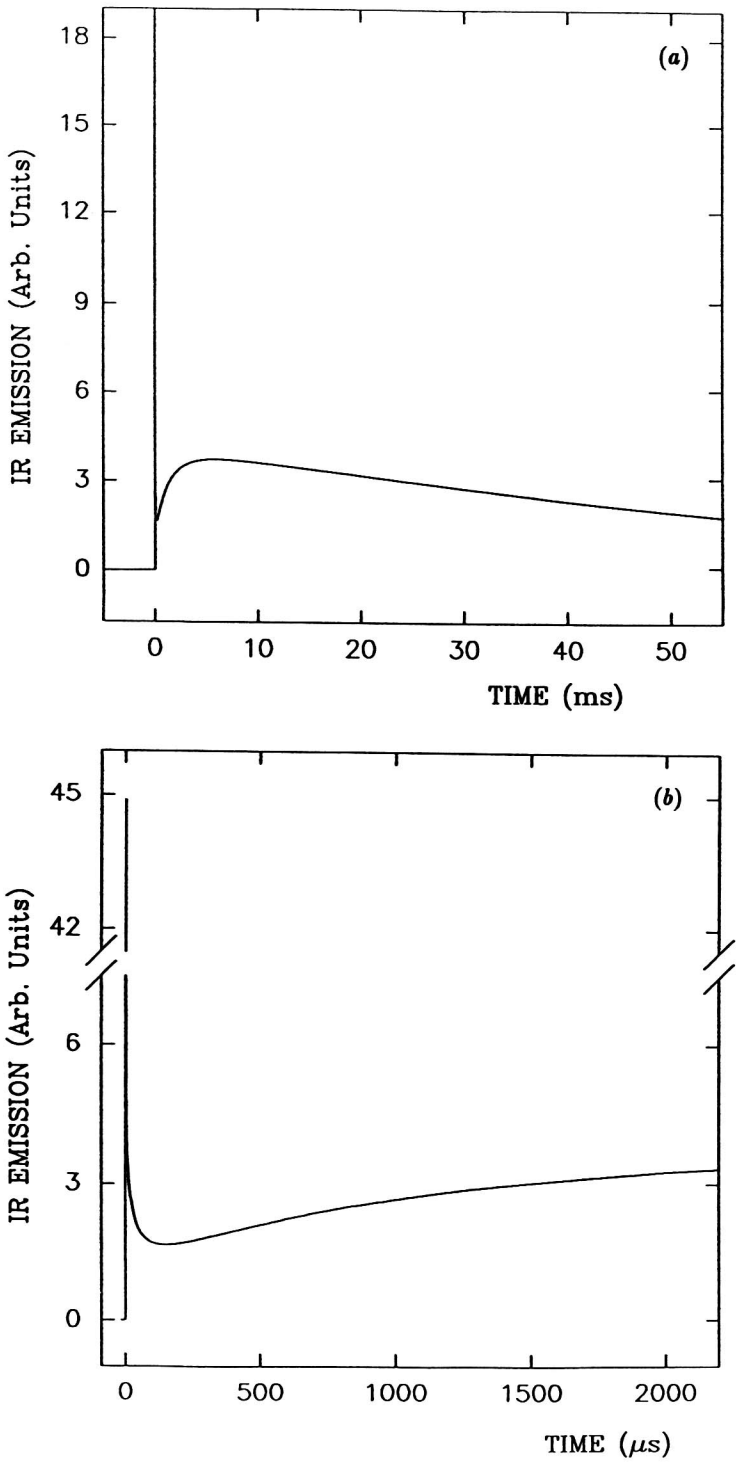

Figure 6. Results of the 3D treatment of the simultaneous conduction–radiation problem, with 1% vol/vol hot-centre loading. $T_h = 5000$ K, $\mu_{IR} = 1000$ cm^{-1}. (*b*) Details of the initial peak.

varied by insertion of volume-absorbing neutral-density filters in the beam path (~ 100–700 mJ cm^{-2} per pulse). A liquid-nitrogen-cooled HgCdTe detector (New England MPC 12-1-8) was placed at the focal plane of a Ge lens to detect the 7.5–14 μm IR emission from a 1 mm^2 area at the centre of the sample's front surface. For measurement of incident fluence, a known portion of light was diverted to an energy meter (Scientech 365) by a beam splitter. The electrical response of the detector, after preamplification, was monitored with a fast digital oscilloscope (LeCroy 9420A), triggered from the output of an Si photodiode (EG&G FND-100) that detected the stray light from the Q-switched laser pulse. The sampling rate of the digital scope was ~ 5 ns/point for early-time studies, and ~ 8 μs/point to examine the long-time effects; data were recorded for 30 000–40 000 points after the trigger. The recorded PPTR signal was then reduced to 200–400 points by averaging. The stability of the system was checked periodically by observing the signal from a neutral-density filter (Schott NG-10) placed at the sample position.

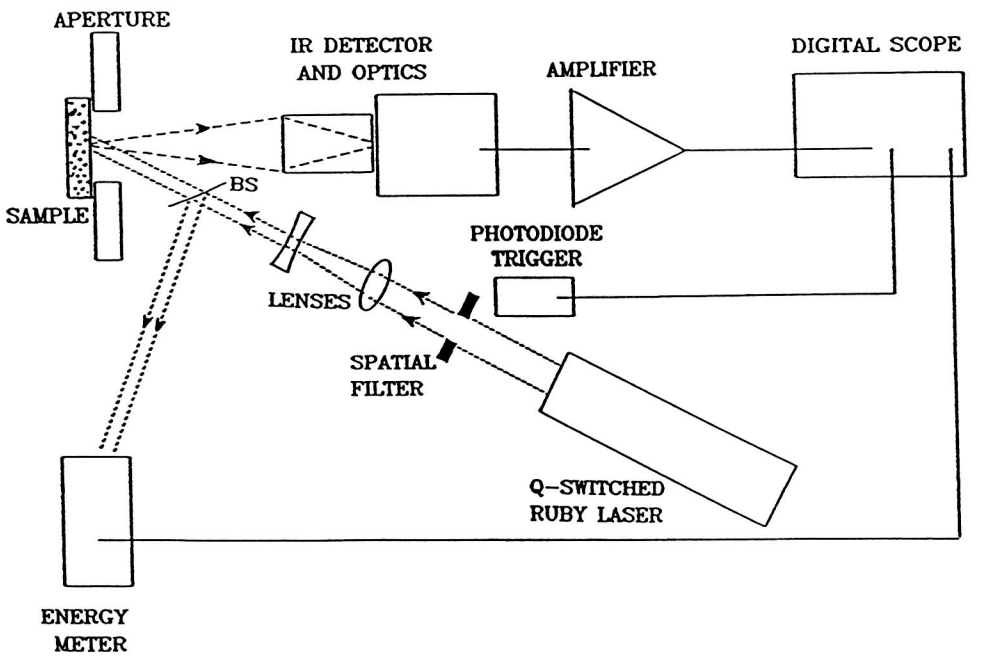

Figure 7. A schematic diagram of the experimental PPTR apparatus. The laser light is incident at ~ 10° from the normal. BS is the beam splitter.

Three different stock dispersions were formed to prepare samples for PPTR measurements. Two consisted of different lots of carbon-black pigment (Ashbury Graphite) mixed with deionized water. The two lots differed primarily in particle size. Lot 1 ('large') had d_{ave} ~ 3.5 μm, and a log-normal size distribution with 75% of particle diameters in the 1.9–4.4 μm range, and lot 2 ('small') had d_{ave} ~ 0.9 μm, and 75% of the particles within 0.6–1.6 μm. Recommended amounts of dispersant (Marasperse BCA-1, Lingotech) were used. The third stock was dry natural melanin powder (Sigma Chemicals). A given stock was gently mixed with a melted collagen gel solution (Knox Gelatine). Small amounts (~ 0.2% vol/vol) of formalin were added to the gel mixture to induce cross-linking in the gel, so that its mechanical strength and melting point were increased. The mixture

was poured into 3.5 cm Petri dishes and allowed to solidify. The finished samples had a smooth-surface black appearance, and were $\sim$ 6 mm thick. Optical transmission, confocal reflectance, and TEM microscopy revealed uniform pigment distribution throughout the gel matrix, with no evidence of settling or conglomeration. The resultant solid concentration in the samples varied from 0.45 to 2.35% (wt/vol).

4. Results and discussion

4.1. Results from carbon-black samples ('large' particles)

Figure 8 shows a typical PPTR signal from a cross-linked collagen gel containing 2.35% of 3.5 μm diameter carbon granules. The detected signal is qualitatively similar to the theoretical predictions of figures 2–6. We can estimate the maximum temperature reached by the carbon particles following the 50 ns laser pulse as follows. Assuming no thermal losses during the pulse duration, the maximum temperature excursion will be

$$T_h \sim \Phi_0 Q_a A/\rho c V \tag{14}$$

where Φ_0 is the incident fluence, A and V are the particle cross-sectional area and volume, and Q_a is the absorption efficiency of the particle. The latter quantity can be calculated using Mie theory (Bohren and Huffman 1983) if the optical constants of bulk carbon are known. Most literature values indicate that $n_{carbon} \sim (1.5\text{–}2.0) + (0.5\text{–}1.0)i$ in the visible (Janzen 1979, Pluchino *et al* 1980). Using these values, and $n_{water} = 1.33$ and $\lambda = 694$ nm, Mie theory predicts $Q_a \sim 1.0$ for all the particle diameters in this sample, so the particle absorbs all the optical energy incident on it. Using $\Phi_0 \sim 400$ mJ cm^{-2}, $\rho \sim 2$ g cm^{-3}, $c \sim 0.70$ J g^{-1} K^{-1}, the expected range of maximum temperature excursions is $T_h \sim 2100$ K ($d = 1.9$ μm), 1150 K ($d = 3.5$ μm), and 900 K ($d = 4.4$ μm). Thus the maximum attainable temperature is inversely proportional to the particle diameter; since the thermal radiative emission depends on the product of particle surface area and the fourth power of temperature, we expect IR emission $\propto d^{-2}$. The dependence of the PPTR signal on the size of the absorbing centres will be discussed later.

The effect of increasing the incident fluence by 50% is shown in figure 9. Compared with figure 8, the initial peak is significantly higher ($\sim$ 35 units against 11 units) and somewhat broader (FWHM $\sim$ 10 μs against $\sim$ 6 μs). Given that $T_h \propto \Phi_0$, and IR emission $\propto T^4$, the experimentally observed increase in the height of the first peak is lower than expected ($11 \times (1.5)^4 \sim 55$). Perhaps there are inaccuracies in using (14) to estimate T_h, or experimental problems in detecting such a large transient signal (for example, photons with $\lambda < 7.5$ μm will not be detected because of the Ge filter, and the fraction cut off will be greater at higher fluences because of Wien's Law (Planck 1959)).

4.2. Effect of absorber particle size

Figure 10 shows a PPTR signal using small-diameter carbon granules. Compared with the spectrum of figure 8, the first peak is higher ($\sim$ 19 units against 11 units) and narrower (FWHM $\sim$ 4.5 μs against 6 μs). Moreover, the second peak is much less pronounced, and occurs at an earlier time ($\sim$ 1 ms). The two features of the first peak are generally consistent with the theoretical predictions for the radiative cooling of a small particle, although a much higher peak would have been expected if indeed IR emission $\propto d^{-2}$ ($11 \times (3.5/0.9)^2 \sim 160$). To examine the cooling mechanism at early times in greater detail, we investigated the PPTR

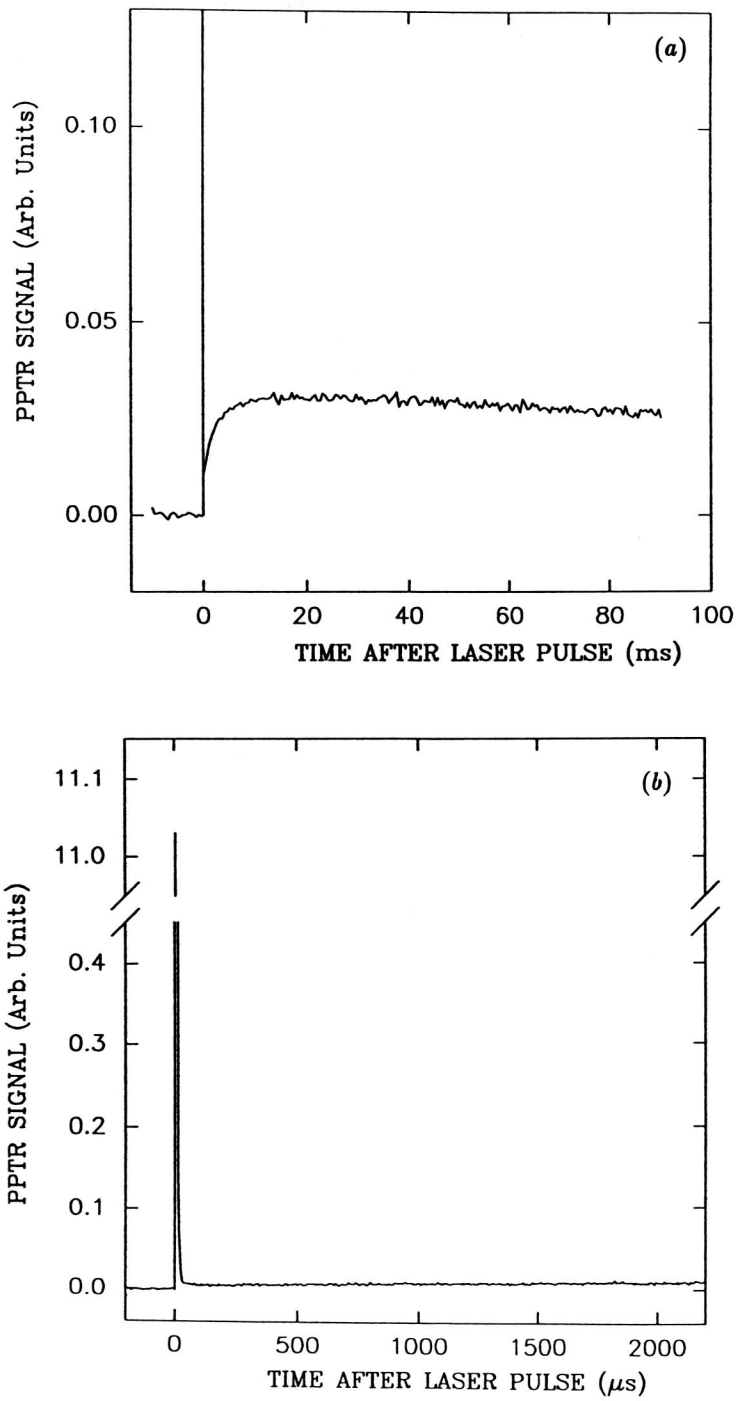

Figure 8. (a) A typical PPTR signal from a water gel phantom containing 2.35% (wt/vol) 'large' carbon-black granules, $d_{ave} \sim 3.5$ μm. The incident fluence was ~ 400 mJ cm^{-2}. (b) Details of the initial peak.

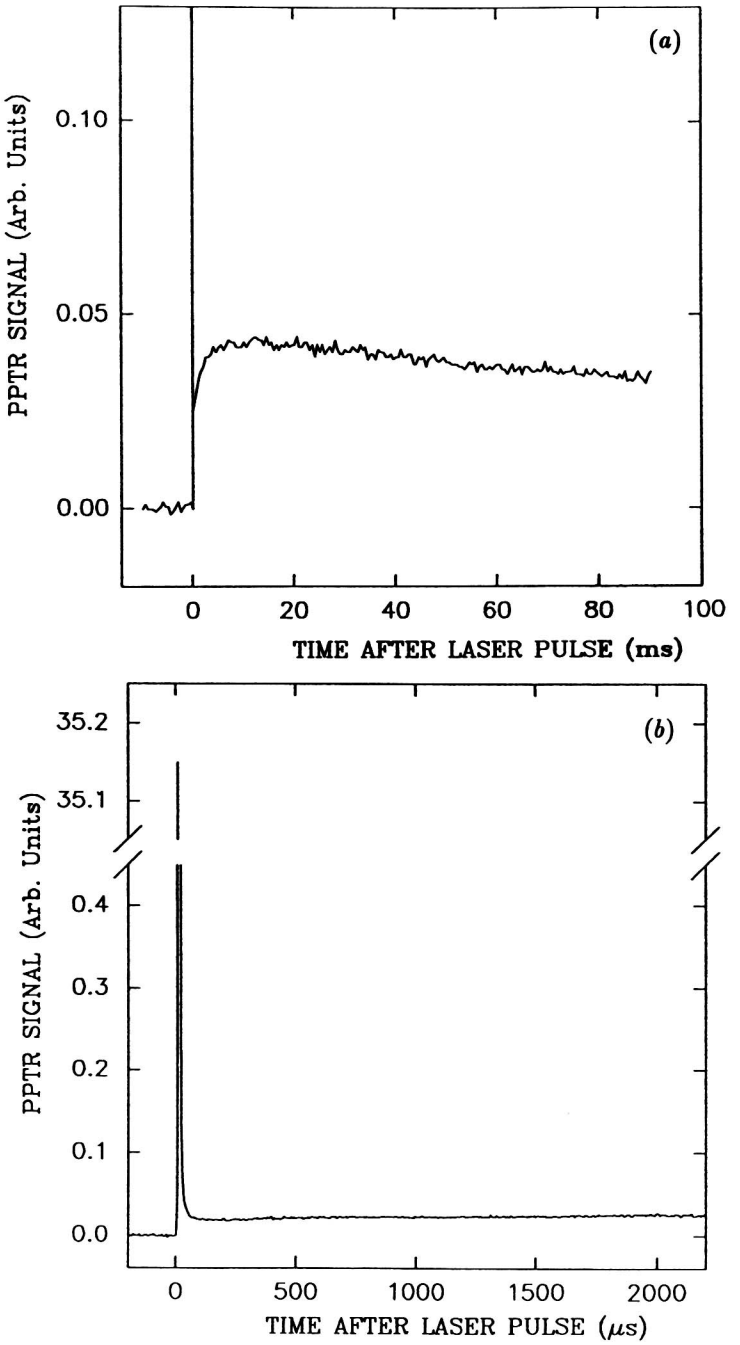

Figure 9. The effect of incident fluence on the PPTR signal. The conditions were as in figure 8, except the incident fluence was ~ 600 mJ cm^{-2}. (*b*) Details of the initial peak.

signal from a water smear containing 0.001% wt/vol carbon powder. The smear was placed on a smooth surface of an IR-transparent window of zinc selenide. The choice of this window material, and of the low pigment loading, was made to simulate single-particle

cooling conditions unimpeded by interactions with other particles or by reabsorption of IR radiation. The results are shown in figure 11. Again, it is seen that the smaller 0.9 μm particles reach a higher initial temperature and cool faster than the larger 3.5 μm particles, but the observed peak height difference ($\sim$ 0.5 against 0.2) again seems relatively slight. One possible reason may be the wide particle-size polydispersity in both carbon samples decreasing the difference between their signals relative to theoretical predictions based on their respective average diameters.

4.3. Possible inaccuracies in estimating the maximum temperature T_h

The early PPTR signal appears to depend less strongly on fluence and on particle size than expected theoretically, suggesting a lower actual maximum temperature level. We therefore examine the validity of our T_h estimate. There are two assumptions inherent in (14): that there is no heat loss from the particle during the heating pulse, and that the absorbed energy is instantaneously distributed throughout the particle. For the first assumption, if the heat loss occurs by conduction, the characteristic time for the cooling process is approximately

$$t_{cond} = d^2/C\alpha \tag{15}$$

where $\alpha = k/\rho c$ is the thermal diffusivity of the surrounding medium, and C is a constant in the range 2–27, depending on the dimensionality of the problem and the definition of the end-point temperature (Hu and Barnes 1970, Anderson and Parrish 1983). Substituting $\alpha_{water} = 0.0013$ cm^2 s^{-1}, the typical cooling times for the three diameters above are $\sim$ 1–6 μs for $C = 27$. Thus, significant conductive cooling does not occur during the duration of the 50 ns laser pulse. However, there is also radiative cooling, which may prevent the absorbing centres from reaching the thermal extremes predicted by (14). The importance of this effect is much more difficult to quantify because of its highly non-linear temperature dependence. Extremely rapid cooling (from $\sim$ 100 K μs^{-1} to $\sim$ 500 K μs^{-1}, estimated from the first microsecond or so of the early peaks of figures 8–10, and from simulation results) implies that the radiative loss also occurs *during the laser pulse*, and the predictions of (14) will be an over-estimate.

The second assumption of (14) is that the energy absorbed within the particle is uniformly and instantaneously distributed throughout its volume. In modelling 'opaque' absorbers, where characteristic dimensions are greater than the optical absorption length, an absorbed energy gradient results. This may produce higher local temperatures than predicted by (14) on the side of the particle facing the incident light. However, if the thermal conductivity and diffusivity of the particle are high, and radiative exchange within it is efficient, the subsequent redistribution and equalization of energy is rapid, especially for micrometre-sized particles (of the order of nanoseconds to microseconds). This absorptive shielding effect underestimates T_h, unlike the above radiative cooling effect (which overestimates T_h), and is also very difficult to quantify. However, the measurements imply lower temperatures than expected, so absorptive shielding does not appear to dominate.

A further possible source of error is the use of constant fluence throughout the medium, and therefore constant T_h, since some of the deeper particles may be partially screened by the overlying absorbers. We, therefore, examined a gel containing 2.35% (wt/vol) of 'large' carbon pigment to which scattering polystyrene microspheres (1.0% wt/vol) were added as light scatterers; these alter the fluence distribution within the gel. The gel phantom appeared cloudy grey, with a similarly smooth surface as seen without the microspheres. There was no significant difference in the PPTR signal from this scattering–absorbing combination,

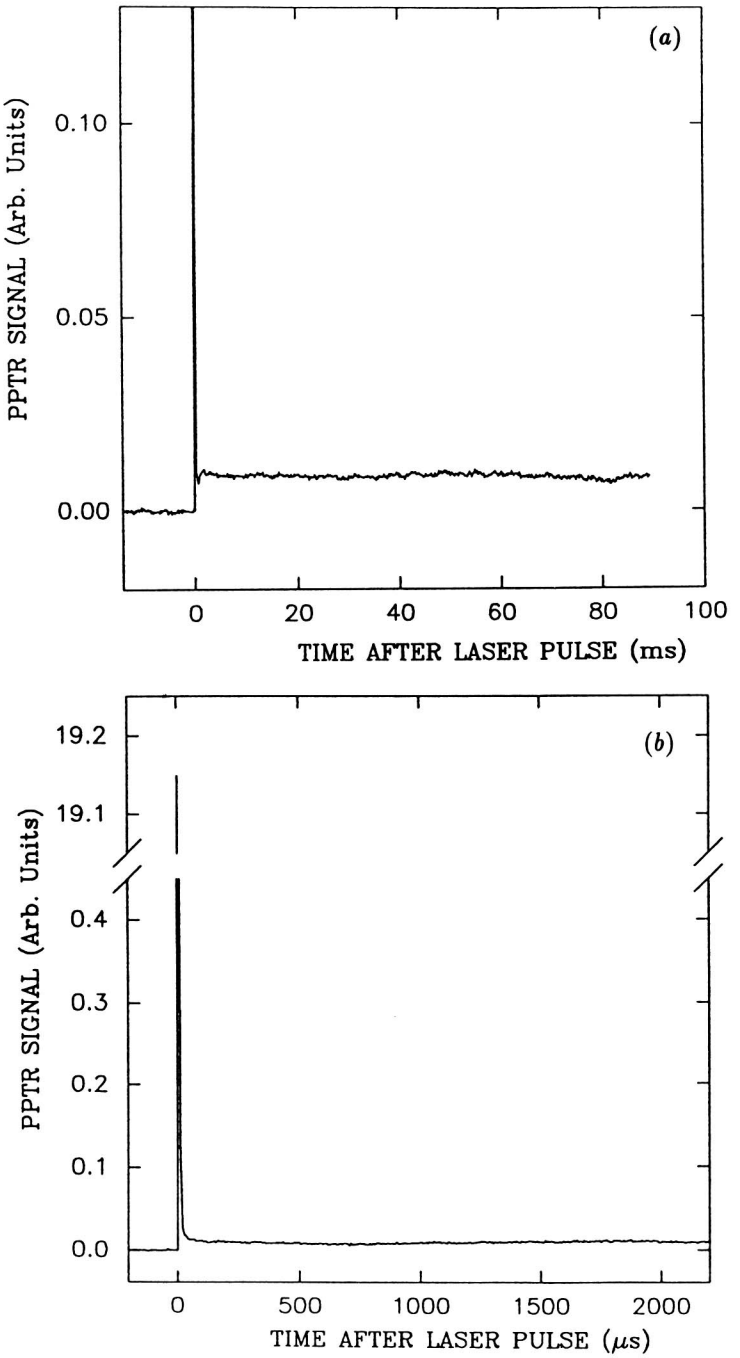

Figure 10. A PPTR signal from a water phantom containing 2.35% (wt/vol) 'small' carbon-black granules, $d_{ave} \sim 0.9$ μm. (b) Details of the initial peak.

implying that alterations in subsurface fluence do not play a major role in the subsequent conduction–radiation transfer, or at least do not influence the radiometric emission from the

material. Thus, to first order, our assumption of equal T_h at all granule locations throughout the volume is adequate for the PPTR model.

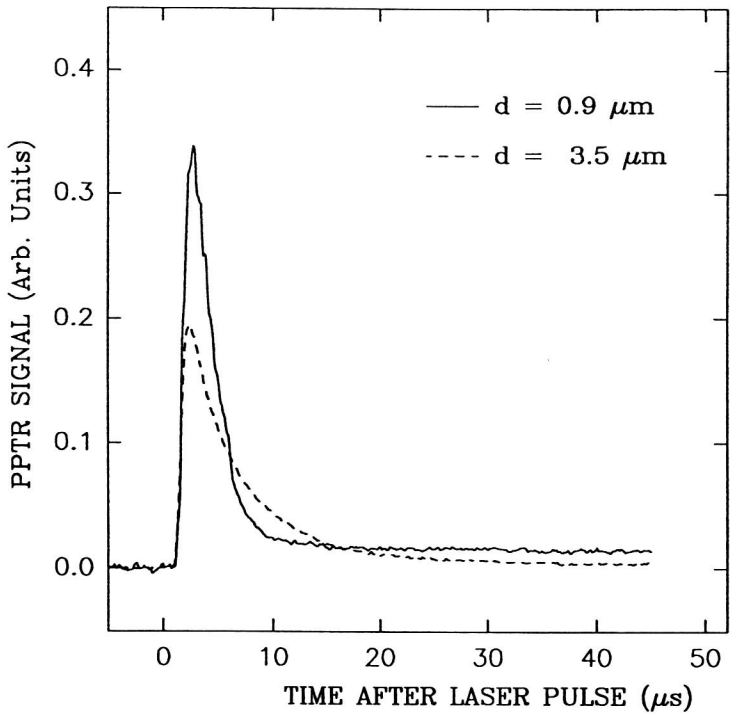

Figure 11. A comparison of the early-time PPTR signals from two wet monolayers containing very tenuous suspensions (~ 0.001% wt/vol) of each of the two carbon particle sizes.

4.4. Results from melanin samples

Figure 12 shows a PPTR signal from an aqueous gel phantom containing melanin powder. The particle size distribution is similar to the 'small' carbon-black samples examined above. However, the signal is dramatically different—the double-peak structure seen before has been replaced by a gradual monotonic decay from the initial maximum. This signal behaviour is characteristic of materials with volumetrically distributed optical absorbers, such as neutral-density filter or a molecular dye solution (Tam and Sullivan 1983, Prahl *et al* 1992). Since the melanin sample is clearly a particulate suspension, there must be some significant differences between the two particle types to account for the different PPTR signals. The thermal properties of the two are similar, within about a factor of ~ 8× (Crippa and Viappiani 1990, Vitkin *et al* 1994c). There is a significant difference between the optical constants in the visible, particularly in the imaginary part of the refractive index: whereas $n_{carbon} \sim 2.0 + 1.0i$, $n_{melanin} \sim 1.6 + 0.1i$ (Kurtz *et al* 1986). However, for the particle sizes tested here, even melanin yields $Q_a \sim 1$. An essential difference is that carbon absorption remains high in the IR (Janzen 1969, Pluchino *et al* 1980, Brewster and Kunimoto 1986), while melanin is essentially IR transparent ($\mu_{IR} \sim 0$) (Wolbarsht *et al* 1982). Thus, its radiative emission term becomes inefficient (5), so the heat initially

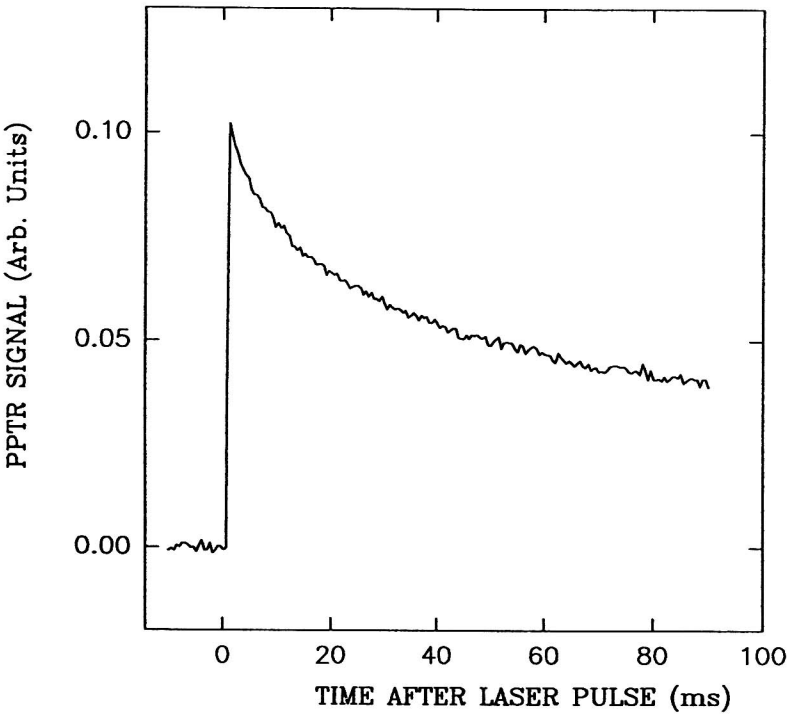

Figure 12. A typical PPTR signal from a water phantom containing 2.35% (wt/vol) melanin powder. The incident fluence is ~ 400 mJ cm^{-2}.

deposited in the melanin granules is not emitted radiatively, either to the IR detector to give the initial PPTR spike, or, more importantly, to the surrounding medium to cool the granule. The dominant cooling must take place by the slower mechanism of conduction to surrounding water matrix. We modelled this situation in figure 13, where the results do indeed display the experimentally seen behaviour. These findings confirm the importance of radiative transfer during the early phase of cooling by IR-emitting particles.

4.5. Effect of medium properties

The assumption of temperature- and wavelength-independent optical and thermal properties of the medium and of the hot centres may be inaccurate in some cases. The highest inaccuracy is likely to result from ignoring the temperature–wavelength dependence of the emission spectrum and of the IR absorption coefficient. The wavelength of the black-body emission maximum is described by Wien's law (Planck 1959); for example, at $T = 300$ K, $\lambda_{max} \sim 9.7$ μm, and for $T = 3000$ K, $\lambda_{max} \sim 1$ μm. The μ_{IR} values used above correspond to the absorption properties of water in the ~ 2–15 μm range. However, as the emission maximum shifts to lower wavelengths at higher temperatures, water transparency below $\lambda \sim 1.3$ μm may become significant. Thus, if the local temperature transient results in a significant visible incandescence flash, this energy fraction will be lost from the sample. Such flashes were observed with the carbon samples but not with the melanin samples. Nevertheless, this is unlikely to be the dominant cooling mechanism because of the high temperatures needed to enable a significant fraction of the energy to be emitted in the visible-to-near-IR range (Ozisik 1973). However, at very early times in samples with high

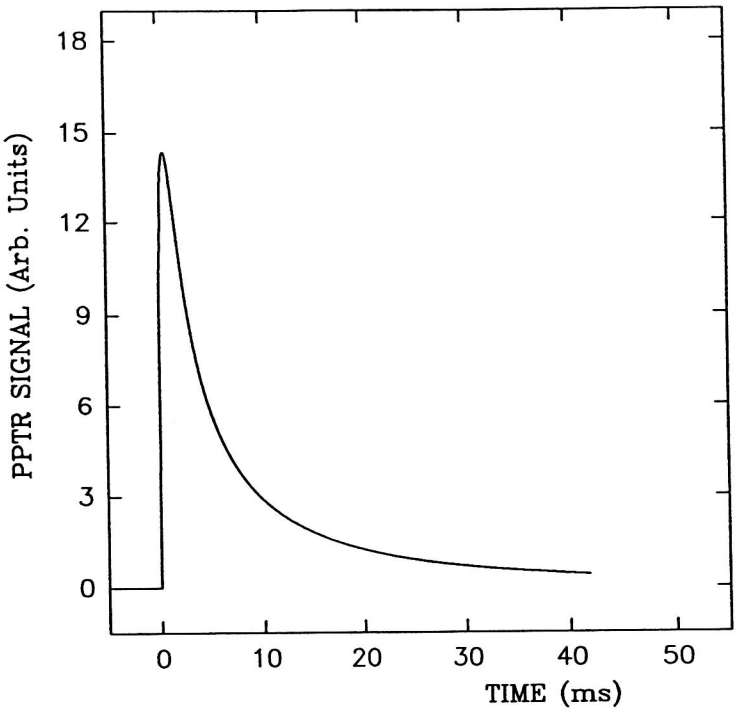

Figure 13. The effect of IR transparency of the hot centres. $T_h = 5000$ K, μ_{IR}(hot centres) = 0 cm^{-1}, μ_{IR}(medium) = 1000 cm^{-1}. Other parameters are as in figure 2.

values of T_h, the spectrally resolved μ_{IR} of the medium (appropriate to the spectrum emitted from the hot granules) is probably smaller than the wavelength-averaged μ_{IR} employed in the simulations.

5. Summary and conclusions

We have studied the transient behaviour of the temperature field in a medium with discrete absorbing centres following a brief laser pulse. The PPTR signal from such a system is so unlike previous published results from experiments with volumetrically distributed absorption that an additional heat transfer mechanism of radiative transfer has been invoked. While radiative transfer has been previously used in PPTR models to account for IR emission from the sample surface, the intramedium heat transfer has always been assumed to follow the laws of heat conduction. Experimental results and theoretical predictions have been compared for a range of particle types, sizes, and initial temperatures. It is seen that radiative transfer becomes more significant with increasing temperatures of the hot centres, with decreasing IR absorption of the medium, and with increasing IR absorption of the particles, implying that thermal confinement becomes difficult for small hot objects. The overall radiative contribution to intermedium heat transfer, and therefore its perturbation of the internal temperature field, appears relatively minor for the range of the examined parameters. It does, however, strongly influence the radiometric emission from the sample, and hence the PPTR signal.

Detailed knowledge of the optical and thermal transfer dynamics is important in modelling and optimizing laser–material interaction in fields such as laser fusion and photomedicine. Pulsed photothermal radiometry, PPTR, a non-contact measurement technique, is well suited to supply this information. The mechanism investigated in this paper to explain some features of the PPTR signals, that of radiative heat transfer within the medium, may become important if the temperature transients reach thousands of kelvin. Application where this may occur include laser ablation of materials, tattoo and pigmented skin lesion removal in dermatology, and pulsed laser therapies in ophthalmology.

Acknowledgments

The authors would like to acknowledge the excellent experimental help of Mr U Bruggemann and Mr W Farinelli, and helpful discussions with Drs T Farrell and M Patterson. IAV thanks the National Cancer Institute of Canada for financial support. This work was supported by the Ontario Laser and Lightwave Research Centre (OLLRC) and by Office of Naval Research grant No N00014-91-C-0084.

References

Al Abed A and Sacadura J F 1983 A Monte Carlo–finite difference method for coupled radiation–conduction heat transfer in semitransparent media *J. Heat Trans.* **105** 931–3

Anderson R R and Parrish J A 1983 Selective photothermolysis: precise microsurgery by selective absorption of pulsed radiation *Science* **220** 524–7

Arpaci M 1962 *Conduction Heat Transfer* (Menlo Park, CA: Addison-Wesley)

Atalla S R and Hassan H F 1986 A modified approach to the conduction–radiation heat transport mechanism in the AC heated strip technique for the measurement of thermal properties of liquids *Proc. 10th Eur. Conf. on Thermophysical Properties (Rome, 1986)* (Rome: ETPC)

Bohren C F and Huffman D R 1983 *Absorption and Scattering of Light by Small Particles* (New York: Wiley–Interscience) appendix A

Brewster M Q 1992 *Thermal Radiative Transfer and Properties* (New York: Wiley–Interscience)

Brewster M Q and Kunimoto T 1984 The optical constants of coal, char, and limestone *J. Heat Trans.* **106** 678–83

Chandrasekhar S 1950 *Radiative Transfer* (London: Oxford University Press)

Crippa P R and Viappiani C 1990 Photoacoustic studies of non-radiative relaxation of excited states in melanin *Eur. Biophys. J.* **17** 299–305

Gerald C F and Wheatley P O 1984 *Applied Numerical Analysis* 3rd edn (Reading, MA: Addison-Wesley)

Goody R M and Yung Y L 1989 *Atmospheric Radiation: Theoretical Basis* 2nd edn (New York: Oxford University Press)

Hu C L and Barnes F S 1970 The thermal–chemical change in biological materials under laser irradiation *IEEE Trans. Biomed. Eng.* **BME-17** 220–8

Imhof R E, Birch D S J, Thornley F R, Gilchrist J R and Strivens T A 1984 Optothermal transient emission radiometry *J. Phys. E: Sci. Instrum.* **17** 521–5

Janzen J 1979 The refractive index of colloidal carbon *J. Colloid Interface Sci.* **69** 436–47

Kobsa P H, Latina M A, Crean E V, Hasan T H, Rakestraw S L and Yarmush M L 1989 Targeting of trabecular meshwork cells by selective phototoxicity *Invest. Ophthalmol. Vis. Sci.* **30** (AVRO Supplement) 222

Kurtz S K, Kozikowski S D and Wolfram L J 1986 Nonlinear optical and electro-optical properties of biopolymers *Electro-Optic and Photorefractive Materials* ed P Gunter (Berlin: Springer) pp 110–30

Leung W P and Tam A C 1983 Thermal diffusivity of thin films measured by noncontact single-ended pulsed-laser-induced thermal radiometry *Opt. Lett.* **9** 93–5

—— 1988 Thermal conduction at a contact interface measured by pulsed photothermal radiometry *J. Appl. Phys.* **63** 4505–10

Ozisik M N 1973 *Radiative Transfer and Interactions with Conduction and Convection* (New York: Wiley–Interscience)

Planck M 1959 *The Theory of Heat Radiation* (New York: Dover)

Pluchino A B, Goldberg S S, Dowling J M and Randall C M 1980 Refractive-index measurements of single micron-sized carbon particles *Appl. Opt.* **19** 3370–2

Polla L L, Margolis R J, Dover J S, Whitaker D, Murphy F G, Jacques S L and Anderson R R 1987 Melanosomes are a primary target of *Q*-switched ruby irradiation in guinea pig skin *J. Invest. Dermatol.* **89** 281–6

Prahl S A, Vitkin I A, Bruggemann U, Wilson B C and Anderson R R 1992 Determination of optical properties of turbid media using pulsed photothermal radiometry *Phys. Med. Biol.* **37** 1203–17

Roider J, Michaud N A, Flotte T J and Birngruber R 1992 Response of the retinal pigment epithelium to selective photocoagulation *Arch. Ophthalmol.* **110** 1786–92

Siegel R and Howell J R 1988 *Thermal Radiation Heat Transfer* 2nd edn (New York: Taylor, Francis, Hemisphere)

Sparrow E M and Cess R D 1978 *Radiation Heat Transfer* (New York: McGraw-Hill)

Sutton W H 1986 A short time solution for coupled conduction and radiation in a participating slab geometry *J. Heat Trans.* **108** 465–6

Tam A C and Sullivan B 1983 Remote sensing applications of pulsed photothermal radiometry *Appl. Phys. Lett.* **43** 333–5

Taylor C R, Gange W, Dover J S, Flotte T J, Gonzales E, Michaud N and Anderson R R 1990 Treatment of tatoos by *Q*-switched ruby laser *Arch. Dermatol.* **126** 893–9

Tom R D, O'Hara E P and Benin D 1982 A generalized model of photothermal radiometry *J. Appl. Phys.* **53** 5392–400

Vance C A, McLeod P J, Reid W H and Ritchie A 1985 *Q*-switched ruby laser treatment of tattoos: a further study *Lasers Surg. Med.* **5** 179–86

Viskanta R and Hirleman E D 1978 Combined conduction–radiation heat transfer through an irradiated semi-transparent plate *J. Heat Transfer* **100** 169–72

Vitkin I A, Wilson B C and Anderson R R 1994a Pulsed photothermal radiometry applications in biological media *Optical–Thermal Response of Tissue to Laser Irradiation* ed M J C van Gemert and A J Welch (New York: Plenum) at press

—— 1994b Analysis of layered scattering materials by pulsed photothermal radiometry: application to photon propagation in tissue *Appl. Opt.* at press

Vitkin I A, Woolsey J, Wilson B C and Anderson R R 1994c Optical and thermal characterization of natural *(Sepia officinalis)* melanin *Photochem. Photobiol.* **59** 455–62

Weast R C and Astle M J (ed) 1983 *CRC Handbook of Chemistry and Physics* 63rd edn (Boca Raton, FL: Chemical Rubber Company)

Wolbarsht M L, Walsh A W and George G 1981 Melanin, a unique biological absorber *Appl. Opt.* **20** 2184–6